Chalcogenide Letters Vol. 19, No. 6, June 2022, p. 389 - 408

Studying the structural, optical spectroscopic ellipsometry and electrical properties of variable-CdS thickness/CdTe for solar cell applications

M. A. Sebak[a,*], S. Ghalab[a,b], Atef El-Taher[c], E. R. Shaaban[c]
[a]*Physics Department, College of Science and Arts, Jouf University, P.O. Box 756, Al-Gurayyat, Saudi Arabia*
[b]*Physics Department, Faculty of Science, Al-Azhar University, Nasr City 11884, Cairo, Egypt*
[c]*Physics Department, Faculty of Science, Al-Azhar University, Assiut, 71542, Egypt*

The structural and optical properties of CdS window layer at different thicknesses in the range of (100-300 *nm*) deposited on pre-cleaned glass substrates (CdS/glasses) via the thermal evaporation process are studied in the current work. The structural analysis is done using Rietveld refinement and atomic pressure microscope techniques. The films of CdS/glass showcase a wurtzite behavior. XRD and AFM tests are confirmed that the structural parameters improve as the thickness of the CdS-layer increases. The optical constants (the refractive index n, the extinction coefficient, k and the bandgap energy values are estimated from spectroscopic ellipsometry (SE) via the construction of an optical model. The refractive index of the CdS/glass films increases with the increase of CdS-layer thickness. This, in turn, is due to the rise of the size of the crystal in the thin layers. It is also found that as the thickness of the CdS-layer rises, so does the overall behavior of the extinction coefficient. Additionally, the bandgap energy of the direct transition decreases from 2.45 eV (*d*=100 *nm*) to 2.25 eV (*d*=300 *nm*). The dark and illumination I-V photovoltaic characteristics of fabricated devices are explored by depositing a p-CdTe thin layer (500 *nm*) over varying thicknesses of CdS thin films (100-300 *nm*) prepared on glass substrates (2 *mm*) and thus, the Ni/n-CdS/i-AgSe/p-CdTe/Pt heterojunction has been successfully fabricated with an AgSe buffer layer deposited directly on the p-CdTe absorber laryer. The n-CdS window layer is deposited on i-AgSe buffer layer. In dark conditions, based on the dependence of the forward and reverse current-voltage, the essential behavior related to the fabricated diode has been determined. As well, in the illumination case, the open-circuit voltage, the short-circuit current, the fill factor, the power conversion efficiency, (*PCE*), photoresponsivity, quantum efficiency, dependence of generated photocurrent on the light intensity, dependence of the generated photocurrent on wavelength (λ)for the studied solar cell are computed and discussed.

(Received March 12, 2022; Accepted June 9, 2022)

Keywords: CdS films, Rietveld refinement, Atomic force microscope, Spectroscopic ellipsometry, Optical constants, Photovoltaic characterization

1. Introduction

As the globe faces the inevitable demise of fossil fuels and severe pollution caused by the fuels, solar energy is emerging as a possible solution to the world energy issue. Among the different methods for producing the sun's energy, solar cells are an efficient method for converting solar energy into usable electrical energy. In 2009, worldwide PV cell and package output were 12.3 GW [1]. One year later, it had risen to more than 20 GW [2].

Semiconductors have received a lot of attention in recent years. The CdS layer is the most fascinating since it has uses in optoelectronics, photovoltaics, catalysis, and biological sensing [3-6]. CdS layer is a semiconductor material with n-type conductivity and an allowed optical bandgap of about 2.45 eV that is commonly used as a window layer in solar cells. Furthermore, the CdS layer has high photosensitivity and so plays a key role in solar cells and other photoelectronic applications [7, 8].

* Corresponding author: masebage@ju.edu.sa
https://doi.org/10.15251/CL.2022.196.389

Because the CdS layer possesses good optical and structural characteristics that qualify it for usage as optical filters, it is also utilized as an insulator as well as a permeable layer for optical beams. Because of the harmony of these properties, this layer uses in a wide range of applications among that [9, 10].

Due to photogenerated charge carriers in the buffer layer are only partially collected, light absorption in the buffer layer (CdS= 2.45 eV) decreases the spectral response of the solar cell inside the blue region of the solar spectrum. The absorption in the cadmium layer of the heterogeneous conduction is identified as a significant contributor to total light loss in polycrystalline thin-film solar cells [11, 12]. However, this loss due to the light absorption is not the only consequence caused by the buffer layer.

Many strategies were mentioned for the deposition of CdS thin films. These encompass thermal evaporation [13], sputtering [10], chemical bathtub deposition [14], spray pyrolysis [15], metal organic chemical vapor deposition (MOCVD) [16], molecular beam epitaxial approach [17], electro deposition [18], photochemical deposition [19] and so forth.

Bonnet *et al.* [20] created the first experimental CdTe/CdS cell in 1972 with 6 percent efficiency, and researchers have labored tirelessly since then to improve the efficiency of such cells. In 2016, the First Solar Company recorded the greatest CdTe/CdS solar cell efficiency of 22.1 % [21].

The thermally evaporated AgSe thin film's structural and optical characteristics were investigated in depth [22]. The optical bandgap for virgin thin films in this investigation was 1.94 eV. This thin film's bandgap energy makes it ideal for use as a window layer/buffer layer for solar cells. On the electrothermal side, the results confirmed that the AgSe thin layer had n-type conductivity [22].

In our current work, we seek to study the photovoltaic properties of a fabricated solar cell as follows: Ni (front electrode)/n-(CdS)/i-AgSe (buffer layer)/p-Si/Pt (back electrode). As previously indicated, heterojunction CdS/CdTe solar cells with superior structural features and solar energy efficiency have been the subject of contemporary study. Surface barriers and surface/interface recombination, however, restrict the performance of CdTe-based solar cells. Our framework develops CdS layers (window layers) and AgSe layer (buffer layers) in a heterostructure based on CdTe-layer (base material/absorber layer) to avoid the obstacles that represented the surface defects, thus ensuring excellent performance and improving the photoconversion efficiency for fabricated solar cells. At the AgSe/CdTe interface, the carrier transport of the AgSe layer creates additional electron-hole pairs. The high light trapping of the CdS layer improves the performance of the AgSe active layer (300 nm-thickness), thereby improving the performance of the fabricated solar cells. In a nutshell, this study looks into the limits of several heterostructures made of CdS, AgSe, and CdTe. The density of defects at the CdS/CdTe interface, which is solved by adding the AgSe layer (the buffer layer) between the CdS (the window layer) and CdTe layer (as the absorber layer) is recombination centers that reduce the performance of such solar cells. This work is not only an extension of the previous series of scientific research on n-CdS/p-CdTe devices, but it is unique from all these works in that it extracts the optical properties for window layers according to an accurate model for calculating the optical constants (spectroscopic ellipsometry (SE)). This model leads to the calculation of the optical bandgap energy along with the optical constants and therefore there is no need for lengthy calculations as used in the usual methods of calculating these quantities. This work deals with the calculation of optical parameters and the precise determination of the structural parameters according to X-ray and atomic force microscopy measurements. The other side of this work focuses on studying the photovoltaic features of the solar cell fabricated at different thicknesses of the CdS-layer. The study of the photovoltaic properties of the generated device is carried out under dark and light conditions. The current-voltage pathway of the forward and reverse bias is discussed in the dark condition and the characteristic parameters of the fabricated solar cells are calculated in the illumination conditions. Among the most important parameters that were addressed in the case of illumination, the open-circuit voltage, the short-circuit current, the fill factor, the power conversion efficiency, (*PCE*), photoresponsivity, quantum efficiency, dependence of generated photocurrent on the light intensity, dependence of the generated photocurrent on wavelength (λ).

2. Experimental details

High purity (99.999%) CdS powder (Alrich chemical compounds organization, USA) became evaporated from molybdenum boat to form the dielectric layer onto ultrasonically cleaned glass substrate kept at regular temperature (150 ^{o}C), using a thermal evaporation unit (Denton Vacuum DV 502 A) and a vacuum of about 10^{-6} Pa. The substrate was circled at a gradual speed of five rpm to gain a uniform CdS thin film. The deposition rate and the film thickness had been controlled using a quartz crystal screen DTM a hundred. The deposition charge was maintained at 2nm/s at some point of the pattern arrangements. The consequences of movie thickness on the CdS thin films have been investigated at 5 distinct thicknesses (100, 150, 200, 250 and 300 *nm*). The films had been evaporated in a nitrogen environment to avoid any oxidation of the film. On the other hand, the method of preparing the AgSe thin film used as a buffer layer was detailed in our recently published work [22].

The constitution of the organized samples has been studied via XRD analysis (Philips X-ray diffractometry (1710)). With nickel-filtered the radiation of Cu Kα that has wavelength = 0.15418 *nm*).The XRD results had been delicate with the aid of the use of the Rietveld method with GSAS-II software [23].

The compositional evaluation of the films checked via (EDXS) technique interfaced to (SEM) (Philips XL) working at an accelerate volt of 30 kV. The error rate in identifying elements was less than 2%. Atomic force microscope (AFM, model MLCT-MT-A) was used to analyze the morphology of the film surface.

The rotating compensator tool (J.A. Woollam, M-2000) was used to measure the SE parameters (ψ and Δ) of the CdS film in the wavelength range of (300-1100 *nm*). Ellipsometric statistics was performed at 70°. All measurements were performed at room temperature. The optical constants of the CdS films have been decided through fitting the version characteristic to the measured information the use of J.A. Woollam Corporation evolved WVASE32 program.

The heterojunction device of the Ni/n-CdS/i-AgSe/p-CdTe/Pt solar cell was fabricated via deposition of the CdTe thin layer (500 *nm*) on the CdS thin films deposited on pre-cleaned glass substrates. The front electrode contact was made by depositing a semi-transparent grid of platinum (Pt) fingers (100 *nm*) directly onto the surface of the CdTe thin leyer, while the back contact electrode was attached to the CdS thin film deposited on the glass substrates, which was nickel (Ni) and had a thickness of 100 *nm*. The front and back electrode contacts were considered ohmic for the small voltages. The current-voltage *I–V* measurements for the generated device were carried out using a standard circuit (Keithley 610 and 617 as a voltage source and current meter) to determine the current through the heterojunction at various thicknesses of CdS. At room temperature, the dark (current-voltage) characteristics were obtained in a completely dark chamber. Under typical test settings, the Keithley 2400 Source Meter device is utilized the global spectra (AM1.5G) to measure the illumination current-voltage (I-V) properties of the solar cell device. The (I-V) features were tested under a specific illumination light source of power (Pin=0.052 (mW/cm^2) to acquire the solar cell parameters. A Chromel-Alumel thermocouple coupled to a digital thermometer was used to immediately detect the temperature. To assess the spectral responsiveness of the fabricated system, a mono-chronometer flawlessly adapted via a rare-gas ion source in the range of (100-1000 *nm*) was utilized, and an electrometer and power temperature gauge to measure the radiation power for the wavelengths and a DC power source with a voltage in the range of (0-15 V) and current in the range of (0-2 A).

3. Results and discussion

3.1. Structural characterization

Fig. 1 illustrates the XRD pattern of CdS powder and the basic simulation test of Rietveld refinement using X'Pert HighSore (version 1.0e) software based on the CdS card. Therefore, the mirror image traces of the CdS powder are attributed to the hexagonal structure (wurtzite type, JCPDS 10-0454) [23-26].

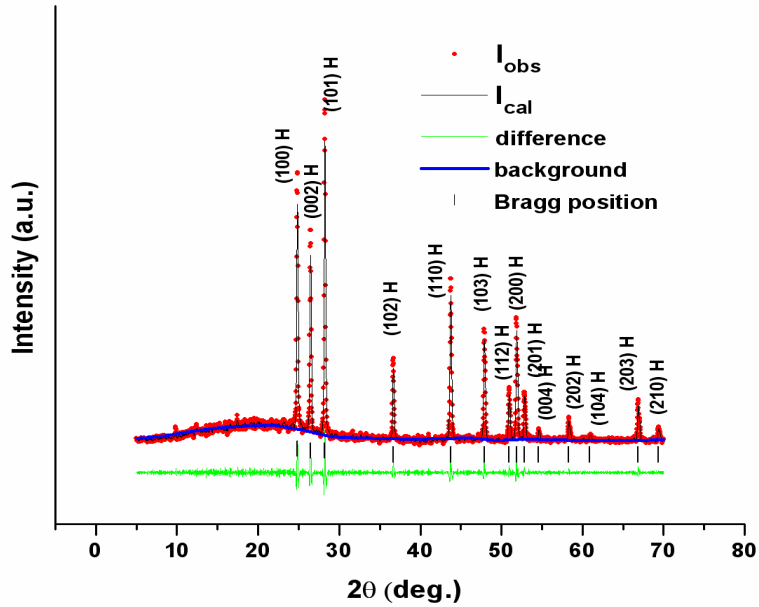

Fig. 1. XRD pattern of CdS powder with Rietveld Refinement.

Fig. 2 displays the XRD of CdS thin film with various thicknesses on glass substrates. The treated samples showed a hexagonal CdS structure with crystal planes (100), (002) and (101). Irrespective of the processing environment, increasing the film thickness results in an increase in peak intensity as the crystallinity of the film rises [27].

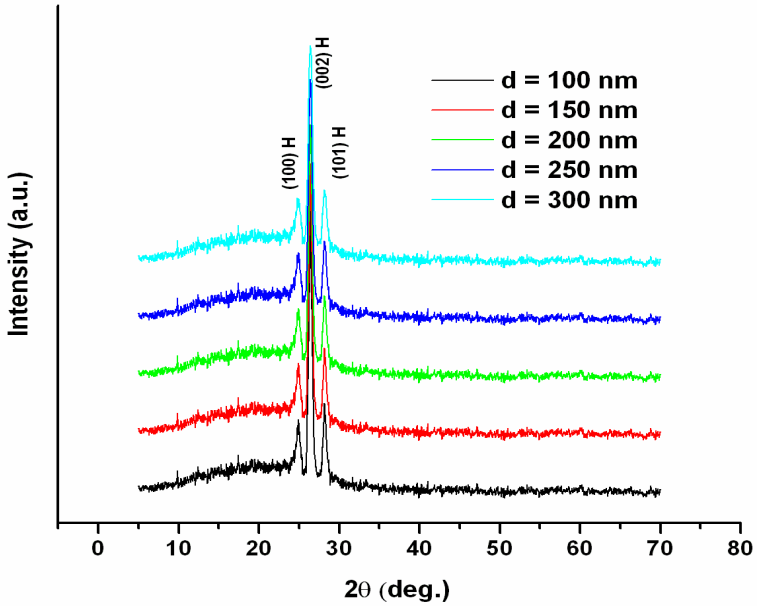

Fig. 2. X-ray diffractograms of the different thickness of CdS thin films.

Then, the crystal structures of thin layers at the different thicknesses were refined in terms of the Rietveld method [22]. The Rietveld refinement are present in Fig. 3 (as an examples). The successful refinement is confirmed by the very small difference between the measured and refined intensities as revealed in Fig. 3 and the low R-factors scheduled in Table 1. According to the refined lattice parameters, as shown in Table 1, the lattice parameter is plotted in Fig. 4. As the thickness of CdS-layer increases, the lattice parameter *a* and c decrease.

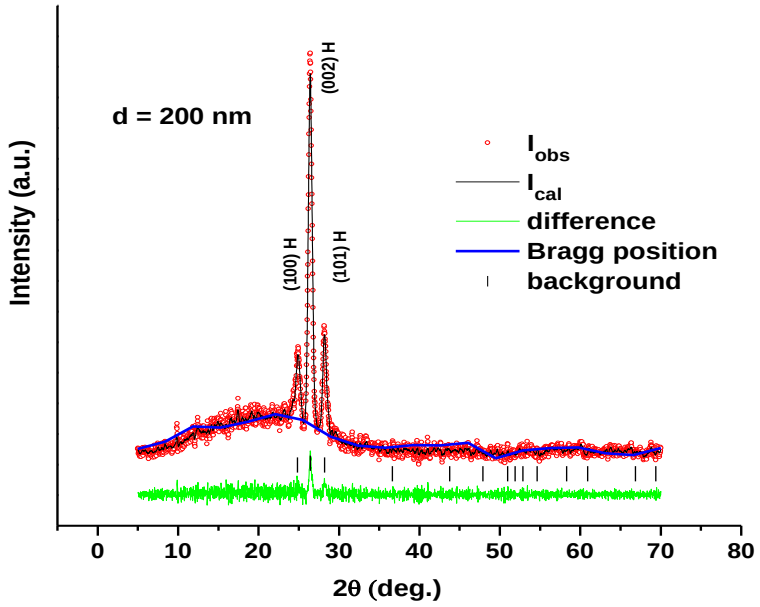

Fig. 3. X-ray diffractograms of 200 nm of CdS thin films with Refinement. By Rietveld.

Table 1. Values of lattice parameters (a and c), volume of unit cell, crystallize size, lattice strain, dislocation density, surface roughness and RMS Surface roughness of different thicknesses of CdS thin films.

d (nm)	***a = b (Å)***	***c (Å)***	***V (Å^3)***	***R-factor***	***Cry. Size (nm)***	***Lattice Str X 10^{-3}***	***Disloc. density X 10^{-4} (lines.nm^2)***	***Surface roughness (nm)***	***RMS Surface roughness (nm)***
100	3.895	6.399	102.354	3.22	16.18	3.95	38	1.526	0.981
150	3.894	6.397	102.240	3.41	18.98	3.89	28	1.761	1.186
200	3.89	6.387	101.956	3.56	22.7	3.76	19	2.552	2.384
250	3.886	6.382	101.672	3.67	25.49	3.56	15	3.066	2.434
300	3.885	6.38	101.559	3.75	26.58	3.34	14	3.626	2.972

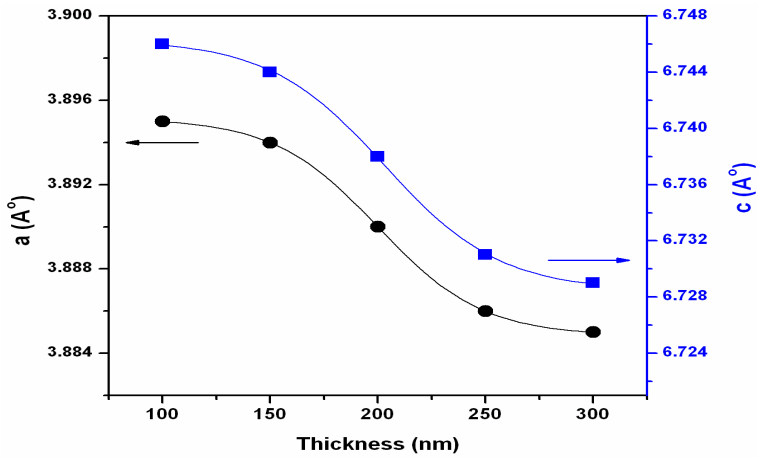

Fig. 4. a and c lattice parameters of a hexagonal CdS thin films in terms of Refinement.

XRD data are additionally analyzed to estimate the scale of crystallite, *D*, and microstrain, ε, of the CdS film with exceptional thicknesses by way of the usage of the Scherrer and Wilson

equations [28-30]. Via analyzing XRD pattern in terms of Scherrer ($D = 0.9\lambda / \beta \cos\theta$) and Wilson equations ($\varepsilon = \beta / 4\tan\theta$) equations [28, 30], both size of crystallite, *D*, and micro-strain, ε are identified with the corresponding correction ($\beta = \sqrt{\beta_{obs}^2 - \beta_{std}^2}$). In which β is the broadening that equals the difference in profile width between the film, β_{obs} and the standard (silicon) β_{std}. The crystallographic properties were highly affected by the presence of dislocation density. The dislocation density is the dislocation lines number per unit area inside the thin film. The crystallite size, *D* related to the dislocation density, δ by the relation (δ=1/D^2). The obtained values of crystallite size, micro-strain, dislocation density and energy bandgap obtained in Table 1. It is found that with enhance of the thickness the mean *D* of the CdS films increment, whereas the micro-strain reduces (see Fig. 5). The rise in crystallite size indicates a reduction in dislocation density and the defects inside the lattice, resulting in decreasing the inner micro-strain. To probable clarify this behavior, higher thickness of the film may additionally mean a better compact stresses in the equivalent film, which can also suggest a much fewer efficient tensile stress and/or strain during the manner of the granule growth, as a result, leading to a larger grain size. The thickness-dependent results of CdS thin films are consistent with those found in previous studies [31-33].

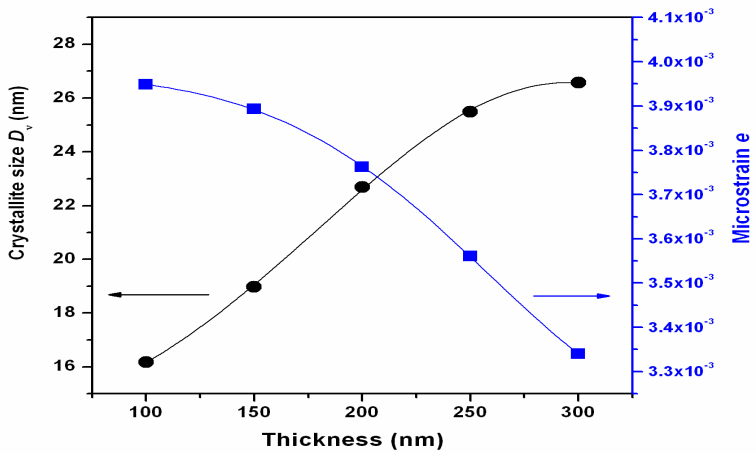

Fig. 5. Crystallite size and lattice strain of CdS nano films.

AFM studies have been used to microscopically describe the surface morphology of CdS layer with different thicknesses. Fig. 6 portrays the three-dimensional (3D) AFM images of the thin layers with 100, 200, and 300 *nm*. The figure illustrates that the surface of the film is clearly dense and evenly arranged. The oriented normal distribution of the elongated grains has similar guidelines, confirming that the positioned favorable orientation grains grow toward the (002) plane. The micrographs of CdS films of different thicknesses were analyzed in detail to determine the microscopic surface morphology parameters, including grain size, surface roughness and root implied rectangular (RMS) surface roughness, as shown in Table 2. The facts indicate that the grain size will increase with increasing the film thickness. However, it was found that the inside roughness and RMS surface roughness increase with the thickness growth.

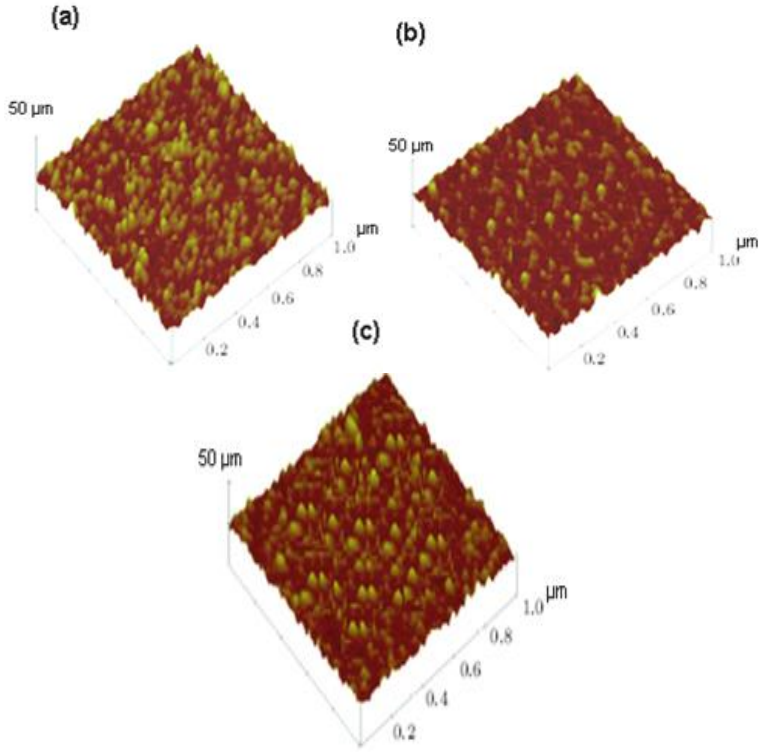

Fig. 6. AFM images of CdS thin films deposited at thicknesses (a) 100 nm, (b) 200 nm and (c) 300 nm.

Table 2. (I-V) and (P-V) parameters of the fabricated solar cells.

d	**Experimental parameters**						
(nm)	V_{OC} **(V)**	I_{SC} **(mA)**	V_{max} **(V)**	I_{max} **(mA)**	P_{max} **(mW/cm^2)**	***FF***	***PCE%***
100	1.262	0.0153	0.954	0.0116	0.0111	57.447	21.345
150	1.425	0.0157	1.120	0.0118	0.0133	59.301	25.595
200	1.579	0.0162	1.273	0.0121	0.0153	60.002	29.498
250	1.763	0.0166	1.439	0.0123	0.0177	60.429	34.071
300	1.935	0.0171	1.596	0.0125	0.0201	60.655	38.483

3.2. Optical properties

Semiconductor thin films have many crucial technical programs, along with optoelectronic device. The presentation of CdS films in large part relies upon on their optical residences and thickness. Spectroscopic ellipsometry (SE) strategies have been used to identify the optical constants precisely. The SE is non-damaging optical strategies, and use layer model to achieve an outcome results.

The spectroscopic ellipsometric outcomes of CdS films evaporated on transparent glass measured by way of SE method changed into within the spectral variety of (300-1100 *nm*) at an prevalence angle of 70°, the information is amassed in intervals of 5 *nm*. The confused mirrored image is eliminated through the use of roughen substrate backs. Spectroscopic ellipsometry without delay information angles Ψ and Δ which can be connected to the complex mirrored or reflected image coefficients (Fresenal's coefficient) of the polarized light by the subsequent equation [34, 35]:

$$\rho = \frac{r_p}{r_s} = \tan\psi \exp(i\,\Delta) \tag{1}$$

Here, Ψ, Δ, r_p and r_s are mentioned the angle received from the amplitude ratio among the parallel polarized wave (p) and perpendicularly polarized wave (s), the polarized waves exchange. The Spectral ellipsometric facts ψ_{exp} & Δ_{exp} of CdS /glass films among a outcome of CdS thickness is provided in Fig. 7.

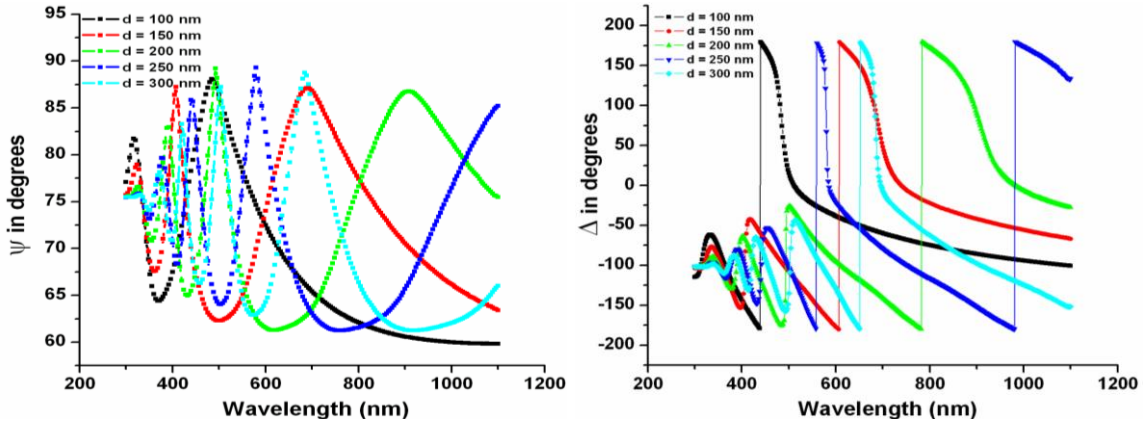

Fig. 7. Ellipsometric parameters data ψ & Δ for of CdS thin films of varies thickness.

The optical values of n, k and d of the CdS films are determined by using least squares regression evaluation and mean square error function (MSE) to change the spectral dependence of ψ_{exp} & Δ_{exp} into the correct version to obtain unidentified fitting parameters and they rely most on borders. The Levenberg-Marquardt regression rule set is completely based on the record matching estimation and the modeling facts of ψ and Δ, and is used to reduce MSE and select the effectiveness of subsequent versions [36, 37]

$$MSE = \frac{1}{2N\text{-}M}\sum_{i=1}^{N}\left(\left(\frac{\psi_i^{mod}-\psi_i^{exp}}{\sigma_{\psi,i}^{exp}}\right)^2+\left(\frac{\Delta_i^{mod}-\Delta_i^{exp}}{\sigma_{\Delta,i}^{exp}}\right)^2\right) \quad (2)$$

In which, M is the appropriate parameters range and N is the number of ψ_{exp} & Δ_{exp} pairs included in the fitting, and that i is the index of summation. The ψ_i^{exp}, Δ_i^{exp} and ψ_i^{mod}, Δ_i^{mod} are called the measured and modeled values, respectively. $\sigma_{\psi,i}^{exp}$ and $\sigma_{\Delta,i}^{exp}$ are the standard deviations of ψ_i^{exp}, Δ_i^{exp}, respectively.

The evaluation of SE records thru non-linear regression evaluation the use of an appropriate optical using Complete Ease SE software program [38]. In the existing examine, the model is built to provide a stacked-layer shape, that's particularly composed of 3 layers: a pitcher substrate, CdS absorber layer, and a rough layer. The rough layer is modeled by using the effective medium approximation (EMA) that is the suitable device to establish the morphology of the multilayer film configuration. More details about EMA are available and described in index [39]. Besides, the glass layer is modeled by using Cauchy version belt in Complete EASE software, while the CdS layer is modeled with the aid of the usage of the B-spline computational process. The B-splines are a recursive set of polynomial splines. More details about polynomial splines noted in details in ref. [40]. Fig. 8 shows the spectral changes of $\psi_{exp.}$, Δ_{exp} of CdS/glass of 300 *nm* CdS layer thickness, which are suited to the calculated ψ_i^{cal} and Δ_i^{cal} data received using the above recommended model. As the thickness of the CdS layer increased from 100 *nm* to 300 *nm*, the fitting process produced a very low MSE value 1.75, and the surface roughness of the CdS film is 3.76 *nm*. In addition, the interference pattern in the spectrum is caused by the coherence of a pair of reflections in the film [41, 42]. The fitted optical constants, namely the refractive index, n and extinction coefficient, k of CdS films with different thicknesses, are shown in Fig. 9 and Fig. 10,

respectively. In addition, it was observed that the refractive index increased with the increase of the thickness of the CdS layer, which was attributed to the rise in crystallinity, which led to the rise in grain size [43, 44]. Fig. 9 shows the k spectral behavior of CdS/glass films with various CdS layer thicknesses obtained from the above model. Obviously, a significantly lower extinction coefficient is observed at the absorption edge, which confirms that the light is absolutely stopped in this variety [45].

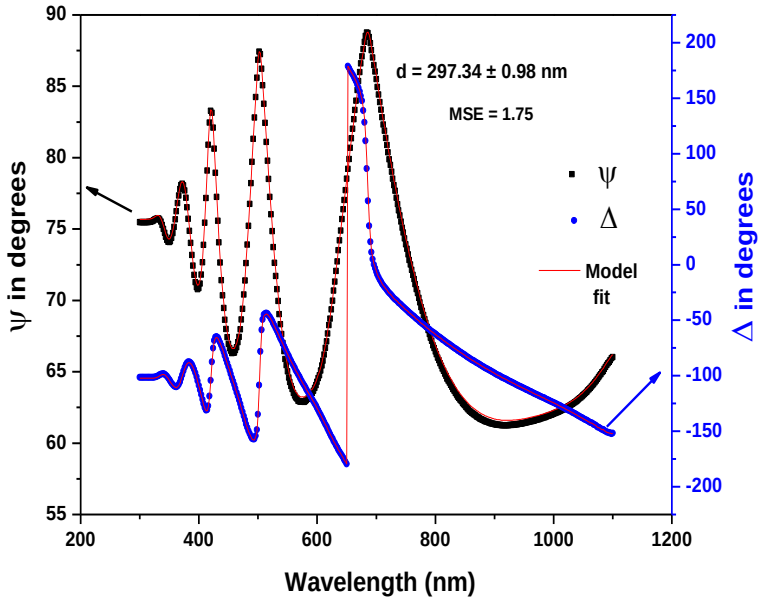

Fig. 8. Ellipsometric ψ and Δ for CdS thin film at 300 nm.Symbols related to and the lines related to fitting.

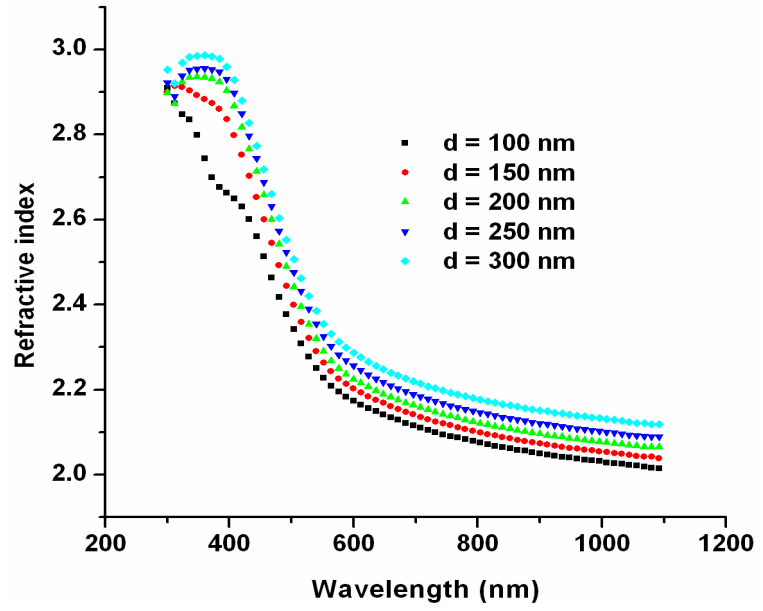

Fig. 9. Refractive index for CdS with varies thicknesses.

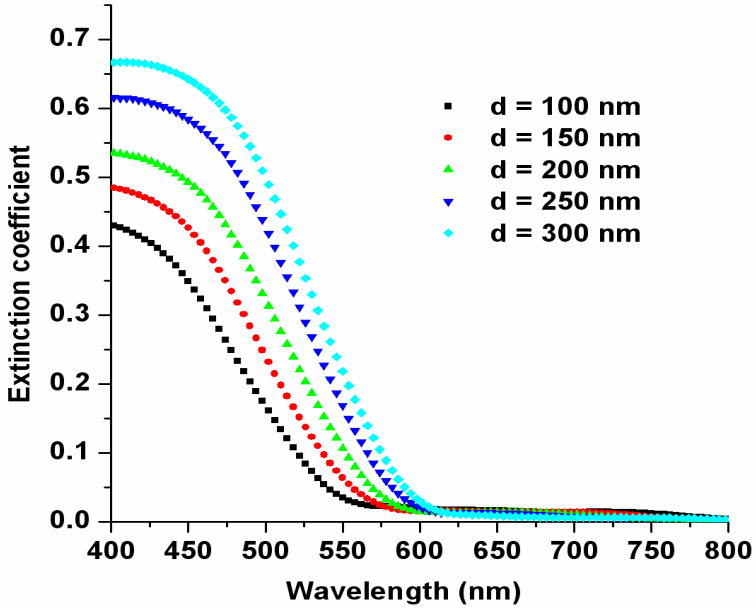

Fig. 10. Spectra of extinction coefficient for CdS of varies thickness.

The absorption coefficient *(α)* of CdS/glass films with diverse CdS layer thicknesses was calculated in terms of k value that extracted from SE model via the subsequent relation [46]:

$$\alpha = \frac{4\pi k}{\lambda} \tag{3}$$

Fig. 11 shows the relationship between α and hν for CdS/glass films with extraordinary CdS layer thickness. As well, the absorption behavior increases as the thickness of the CdS layer increases, especially in the UV range [47]. In addition, the non-zero value of light absorption observed at energies less than the original absorption edge is owing to light absorption at the grain boundaries [48, 49].

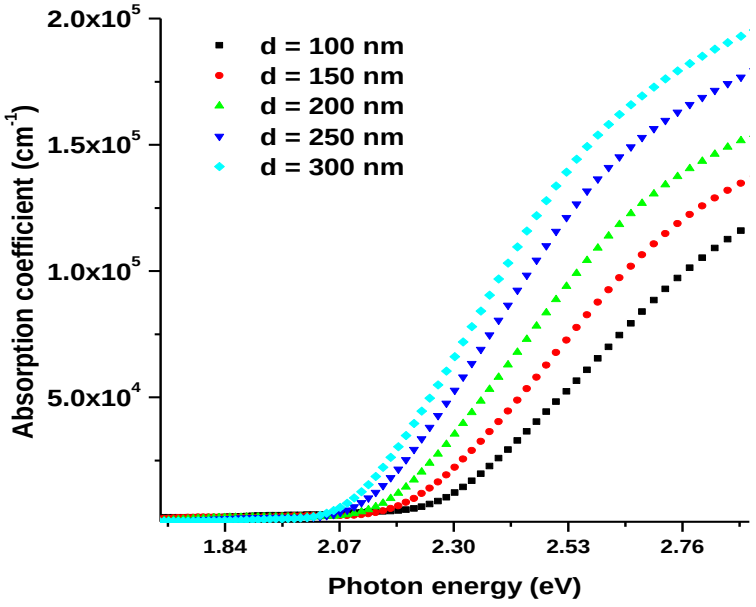

Fig. 11. Absorption coefficient versus photon energy of with different thickness of CdS films.

At strong absorption region, where $\alpha > 10^4$ cm^{-1}, The optical energy band gap E_g^{opt} of varies thicknesses of CdS can be calculated using the Tauc relation of the following expression can be used [50]

$$(\alpha h\nu) = \alpha_o (h\nu - E_g)^p \quad (4)$$

where, α_o and p are constant and exponent. Eq. 4 is the one that determines the type of optical transformations, whether they are allowed or not, depending on the value of the p-value; since the CdS film is polycrystalline, as shown by X-ray diffraction, the transition will most likely be permissible i.e. a p value of half (p = 1/2) [51-54]. Fig. 12 illustrates the relationship of $(\alpha h\nu)^2$ on the vertical axis with $h\nu$ on the horizontal axis of different thicknesses of CdS layer. The value of the gap energy, E_g^{opt} is determined by extending the line part of $(\alpha h\nu)^2$ to cut the horizontal axis, $h\nu$ at a zero value of $(\alpha h\nu)^2$, which is the value of the gap energy. Fig. 13 incarnates the energy gap values as a function of CdS film thickness. It is observed that the value of CdS/glass film decreases as the thickness of the CdS layer increases. Various information have been published to explain that the bandgap decreases with the increase of film thickness, such as the quantum size effect [55, 56], structural parameters [57], the appearance of impurities [58, 59] and the reduction of stress and potential density of dislocations [60, 61]. In this study, the observed decrease in the optical E_g^{opt} of CdS/glass films with the increase in CdS layer thickness is attributed to structural and microstructural parameters e.g. increment in particle size, the reduction in lattice parameters, and lattice micro-strain. In this study, the observed decrease of E_g^{opt} for CdS/glass films with increasing thickness of CdS layer is attributed to the change in microstructures e.g. diminish in lattice parameters, enlarge in crysallize size, and fine lattice compaction [62, 63].

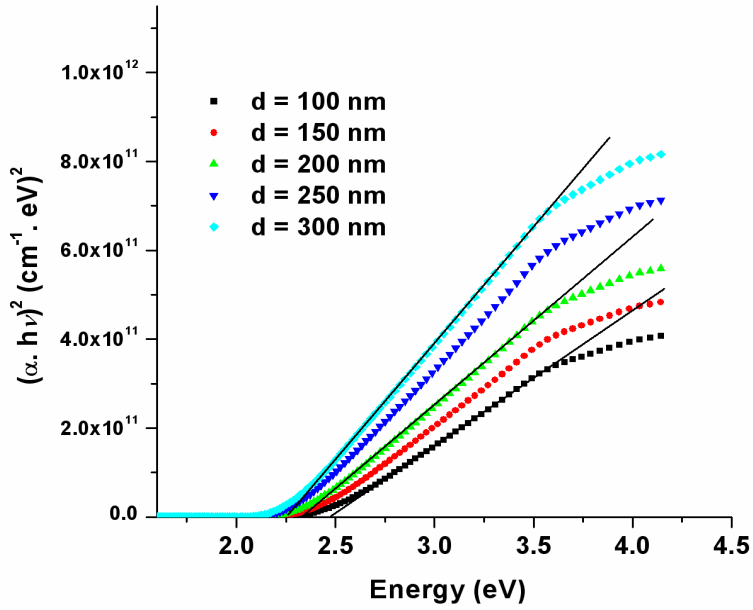

Fig. 12. Variations of $(\alpha h\nu)^2$ versus photon energy $(h\nu)$ for CdS films with different thickness.

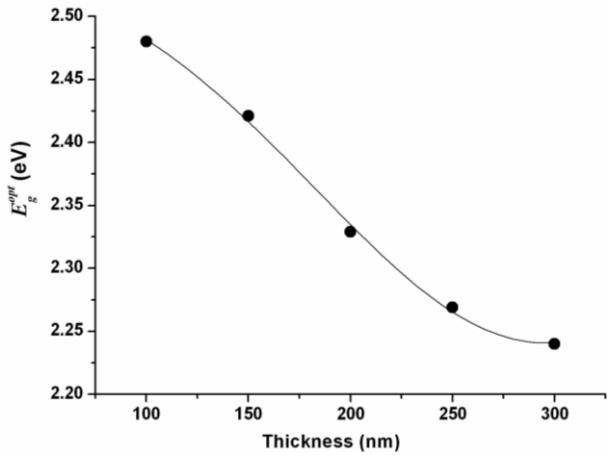

Fig. 13. Energy gap, E_g^{opt} as a function of thickness of CdS thin film.

3.3. Photovoltaic characteristics for fabricated solar cell

The main parameters of the fabricated solar cells are extracted in this work in the temperature range of (100-300 nm) to determine the behavior of dark I-V characteristics for the forward and reverse bias. The diagram of studied n-i-p junction is illustrated in Fig. 14.

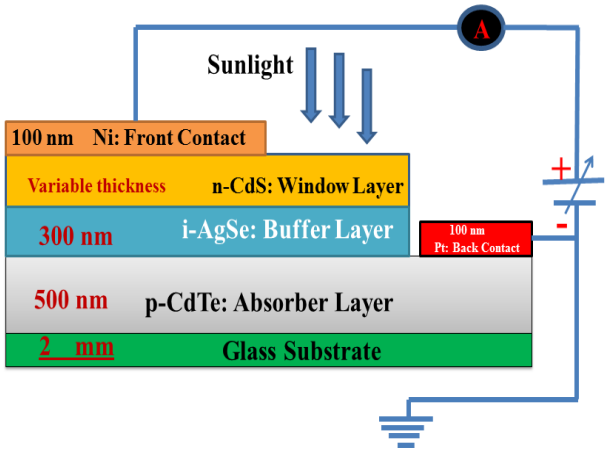

Fig. 14. The diagram of studied n-CdS/i-AgSe/p-CdTe solar cells.

The current I is related to the applied voltage V and the rest of the parameters of the fabricated diode by the following famous equation [64]:

$$I = I_{01}\left(\exp\left(\frac{q(V - IR_s)}{n_1 k_B T}\right) - 1\right) + I_{02}\left(\exp\left(\frac{q(V - IR_s)}{n_2 k_B T}\right) - 1\right) + \left(\frac{V - IR_s}{R_{sh}}\right) \quad (5)$$

In this formula: I_0 symbolizes the saturation current, n epitomizes the quality factor of the fabricated diode), q is the electronic charge which equals to $(1.6\times10^{-19}\ C)$ and k_B recaps the Boltzmann's constant. The rest parameters in **Eq. 5** represent the parasitic resistances which includes the shunt resistance R_{sh} and series resistance R_s .

3.3.1. Energy band diagram of n-CdS/AgSe/p-CdTe heterostructure

Firstly, the band structure feasibility of the n-CdS/i-AgSe/p-CdTe heterojunction for solar cell application has been examined. The corresponding positions of the conduction and valence band edges of CdS (as window layer), AgSe (as buffer layer), and CdTe (as absorber material) are depicted in **Fig. 15**.

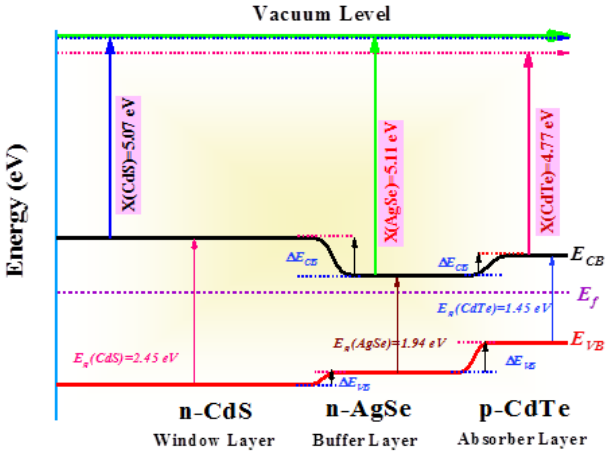

Fig. 15. Energy band diagram of of n-CdS/i-AgSe/p-CdTe heterojunction for CdS-layer with 100 nm.

The following formulae have been used to obtain the level of energy positions for the valence and conductivity bands (E_{VB} , E_{CB}) for the mentioned layers [65, 66]:

$$\left.\begin{aligned}\Delta E_{CB} &= \left(E_C - X + \frac{E_g}{2}\right)\\ \Delta E_{VB} &= \left(E_C - X - \frac{E_g}{2}\right)\end{aligned}\right\} \tag{6}$$

where,

$$X\,(CdTe) = \left(\left(\frac{E_{EA}+E_{Ion}}{2}\right)^{50}_{Cd} \cdot \left(\frac{E_{EA}+E_{Ion}}{2}\right)^{50}_{Te}\right)^{0.01} \tag{7}$$

$$X\,(AgSe) = \left(\left(\frac{E_{EA}+E_{Ion}}{2}\right)^{50}_{Ag} \cdot \left(\frac{E_{EA}+E_{Ion}}{2}\right)^{50}_{Se}\right)^{0.01} \tag{8}$$

$$X\,(CdS) = \left(\left(\frac{E_{EA}+E_{Ion}}{2}\right)^{50}_{Cd} \cdot \left(\frac{E_{EA}+E_{Ion}}{2}\right)^{50}_{S}\right)^{0.01} \tag{9}$$

In the above equations, E_{EA} portrays the electron affinity of single element or material, $E_{Ion.}$ incarnates the first ionization energy, and E_g represents the bandgap energy, (the energy bandgap of CdTe layer and AgSe is 1.45 and 1.94 eV as we mentioned. The (E_{EA} , E_{Ion}) values: for *Cd* (-0.7, 8.99 eV) [67, 68], Te (1.970, 9.009 eV) [67, 69], S (2.077, 10.36 eV) [70, 71], Ag (1.304, 7.57 eV) [72, 73], Se (2.02, 9.75 eV) [73, 74] and the E_C value is 4.5 eV [75].

Based on the relative positions of the band edges of these layers, fabricated solar cells are all efficient and applicable because the levels of the edges of the energy of all the layers ensure

that the energy does not escape and is not lost by the recombination of the different charge carriers in the depletion region. In Fig. 15, the buffer layer (AgSe) has a higher electron affinity compared to the absorber material (CdTe) and this aids to avoid the energy spike at the AgSe/CdTe interface. On the other side, there is also no energy surge at the CdS/AgSe interface (CdS with 100 nm-thickness). This is because the electron affinity for the two mentioned layers is close to each other, as well as the window layer's conductivity is higher than the buffer layer, and the graded junction between them occurs, in which band edges shift over a finite distance with a finite slope proportional to the electric field strength. Furthermore, the n-type CdS at 100 nm-thickness totally exhausts the electrons at the interface, resulting in improved band bending in AgSe, while the p-type CdTe exhausts the holes, resulting in elevated downward bending and the formation of n-CdS/AgSe and AgSe/CdTe interface barriers, as demonstrated in Fig. 15. Moreover, as the voltage drops, the electrons migrate to the p-CdTe region. The holes jump across the barrier at the CdTe/AgSe interface and move into the n-CdS layer. As a result, more charge carriers flow through the heterojunction, increasing the output current for the fabricated device.

3.3.2. The pathway of (current-voltage) dependence

Fig. 16 depicts the dark (*I-V*) features for the manufactured diode in forward and reverse bias for the variable thickness of CdS and applied voltage in the specified ranges. It will be clear from this figure that the current increases as the thickness of the film increases. Fig. 17 portrays the dependence of the current on the applied voltage in the forward bias and reverse bias to highlight the success of the studied solar cell synthesis with high efficiency so that the current in the forward bias is higher than the current in the reverse bias *I-V*. These graphs depict the increase in the current behavior of the generated solar cell in the case of the forward bias, which increases dramatically in the low voltage region. The development and formation of a depletion (exhaustion) region between the CdS thin film formed on the glass substrate and the CdTe thin film deposited on it is related to the exponential behavior in the low voltages. It should be observed that the exponential behavior of the reverse current of the examined manufactured solar cell in the depletion region, i.e. in the low voltage region, is lower than the exponential behavior of the forward current in the same region. As a result, the fabricated solar cell can be said to have exceptional rectification characteristics [76-78].

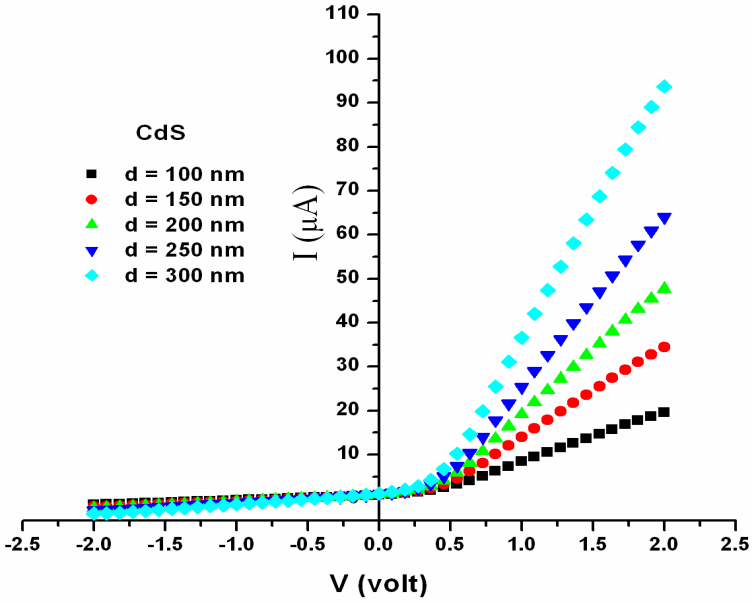

Fig. 16. The dark (I-V) characteristics for the fabricated solar cells.

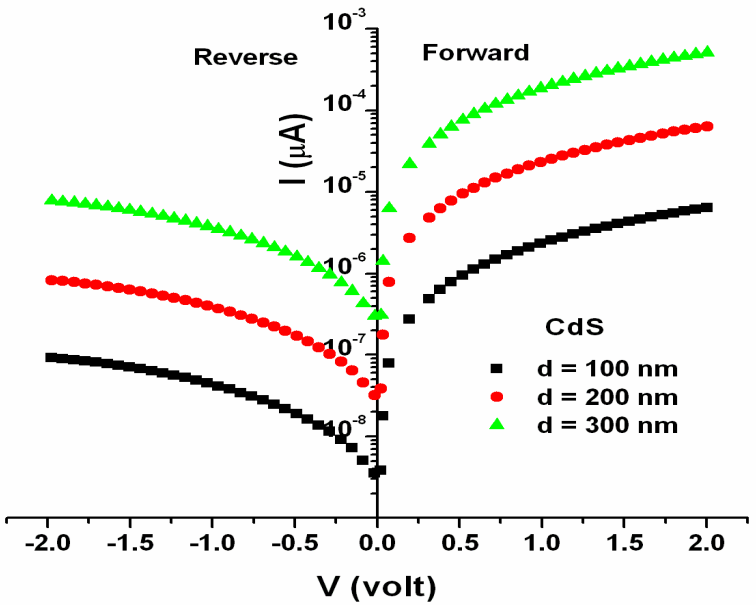

Fig. 17. Current versus the applied voltage for the p-n junction of solar cell at various thickness of CdS in the range of (-2, 2) volts.

3.3.3. Illuminated (I-V) and (P-V) characteristics of fabricated devices

Fig. 18 (a, b) portrays the illuminated *I-V* characteristics of CdS/AgSe/CdTe solar cells with CdS-layer at different thicknesses while Fig. 19 (a, b) incarnates the illuminated *P-V* characteristics.

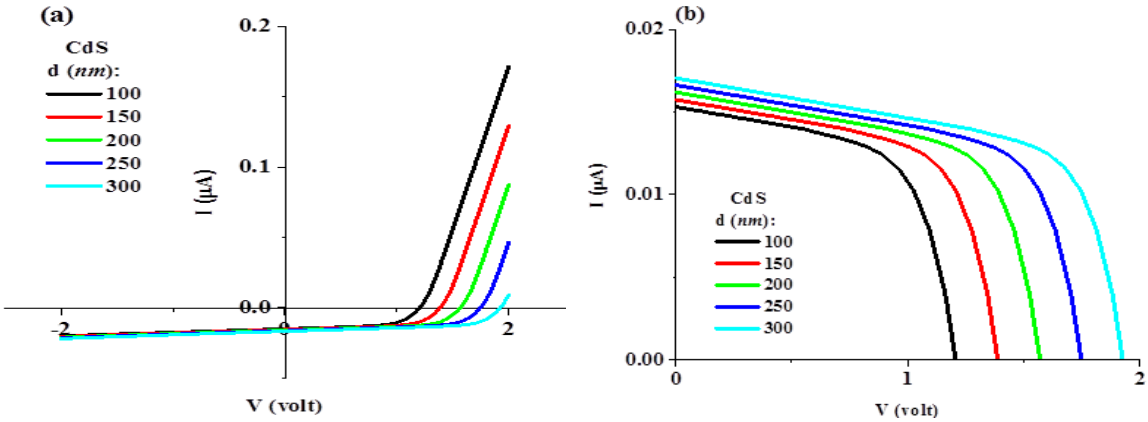

Fig. 18. Illuminated (I-V) curves for the fabricated solar cell at various thicknesses for CdS-layer a) in the range of (-2-2 volt) b) in the range of (0-2 volt).

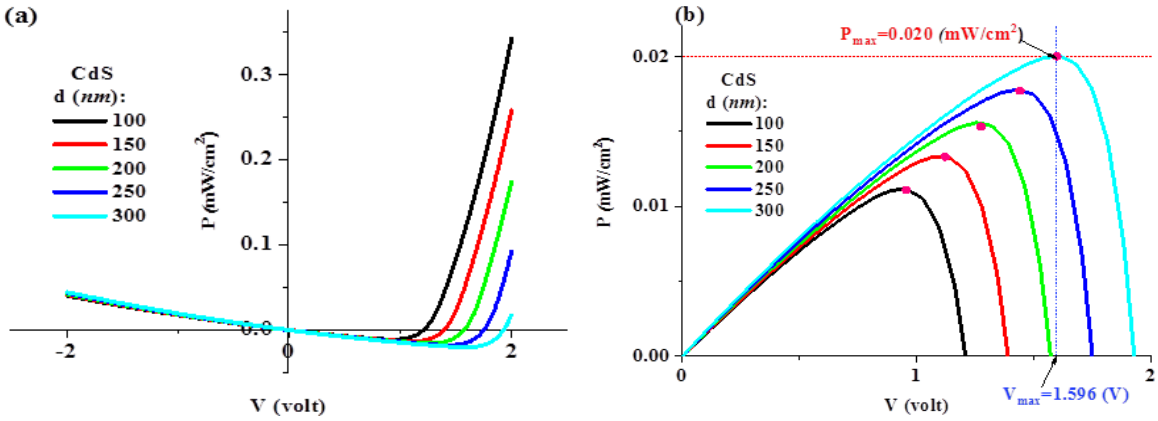

Fig. 19. Illuminated P-V curves for the fabricated solar cell at various thicknesses for CdS-layer a) in the range of (-2-2 volt) b) in the range of (0-2 volt).

The open-circuit voltage V_{OC} and the short-circuit current J_{SC} are determined from Fig. 19 (b). Thus, the power conversion efficiency (*PCE*), which is the ratio of output power, $P_{\max}$ to incident optical power P_{in} (in current work, $P_{in} = 0.052$ (mW / cm^2) is computed from the following formula [79, 22]:

$$PCE = \left(\frac{P_{\max}}{P_{in}} \right) \% \tag{10}$$

As well, solar cells rely on a critical factor known as the "fill factor," which is described as the ratio of maximum attainable power to the ratio of open circuit voltage and short circuit current, as shown below [79, 22]:

$$FF = \left(\frac{V_{\max} . J_{\max}}{V_{OC} . J_{SC}} \right) = \frac{P_{\max}}{V_{OC} . J_{SC}} \tag{11}$$

The obtained values for all mentioned parameters are summarized in Table 2. From this table, one can notice that the highest power conversion efficiency (*PCE*) is 38.48% for CdS-layer with 300 *nm*. We speculate that this improvement in device performance may be related to the high value of transmission and lower reflection at this thickness of CdS-layer. Besides, the Jsc of solar cells at 300 *nm* is slightly higher than that of the rest layers. This behavior may be due to the improvement of optoelectronic properties because the larger amounts of photons are absorbed into CdS/AgSe/CdTe solar cells due to the decrease of reflectance, which leads to the generation of more photo generated carriers in absorber layer and further enhances V_{OC} and J_{SC} . In addition, the possible reason for the relatively high V_{OC} and J_{SC} may be due to the better crystal quality and larger grain size, as well as lower resistivity. The lower resistivity of 300 *nm* CdS-layer compared with the rest layer also contributes to the improvement of the *FF*. This is due to decrease resistance of CdS/AgSe/CdTe solar cells. Combining with the above analysis, it can be concluded that 300 *nm* CdS-layer is beneficial for the improvement of *PEC* for CdS/AgSe/CdTe solar cells.

4. Conclusions

The current study led to important results in the structural and optical aspects of the Cds-layer at different thicknesses, and results related to the fabricated solar cells. With regard to the structural properties of the CdS-layer, it was found that by increasing the thickness of the layer, the size of the crystals improves and the stress caused by the accumulation of atoms on the surface of the thin layer decreases. On the other hand, the spectral spectroscopic ellipsometric (SE) model was used to calculate the optical constants (the refractive index and the extinction coefficient), which were improved thanks to the increase in the thin layer. The optical gap energy was calculated and found to be decreased and this was attributed to the increase of defects in the matrix of the studied system with increasing thickness.

The increase in local defects is a measure of the degree of random arrangement of the atoms in the system, but what happened here is that the distance at which the evaporation took place was fixed at 17 *cm*, which is the distance between the source of evaporation and the substrate. This resulted in the regularity of the atoms as a result of the regularity of the deposition rate and obtaining homogeneous thin films because of controlling the temperature of the substrate during evaporation at a fixed limit. Eventually, the crystallization size increased and this was confirmed by X-ray and by atomic force microscopy techniques. The photovoltaic features had a great section in this study as well, as the dark (current-voltage) characteristics were studied for the fabricated device, and the device behavior in the cases of forward and reverse bias were discussed. On the other hand, the current-voltage and power-voltage properties of illumination conditions were investigated. In this case, the open-circuit voltage, the short-circuit current, the fill factor, the power conversion efficiency, (*PCE*), photoresponsivity, quantum efficiency, dependence of generated photocurrent on the light intensity, dependence of the generated photocurrent on wavelength (λ) for the studied solar cell are computed and discussed. The highest energy conversion efficiency was obtained for the thin layer with a thickness of 300 *nm*, and the value was about 38.48%, which is a high value if compared to previous studies.

Acknowledgments

This work was produced with the financial support of the Dean of Scientific Research of Jouf University: Grant Agreement No (DSR-2021-03003170).

References

[1] Hirshman, W. P., Photon International (2010): 176-199.

[2] Sharma, A., IMS Research (2011): 90-95.

[3] X. Mathew, J. Pantoja Enriquez, A. Romeo, A.N. Tiwari, Sol. Energy 77, 831 (2004); https://doi.org/10.1016/j.solener.2004.06.020

[4] R. K. Sharma, K. Jain, A.C. Rastogi, Curr. Appl. Phys. 3, 199 (2003); https://doi.org/10.1016/S1567-1739(02)00201-8

[5] B. Ullrich, J. W. Tomm, N. M. Dushkina, Y. Tomm, H. Sakai, Y Segawa, Solid State Commun. 116, 33 (2000); https://doi.org/10.1016/S0038-1098(00)00267-2

[6] Han, J., Spanheimer, C., Haindl, G., Fu, G., Krishnakumar, V., Schaffner, J., Fan, C., Zhao, K., Klein, A., Jaegermann, W.: Sol. Energy Mater. Sol. Cells, 95, 816 (2011); https://doi.org/10.1016/j.solmat.2010.10.027

[7] Kim, H., Kim, D.: Sol. Energy Mater. Sol. Cells, 67(1-4), 297 (2001); https://doi.org/10.1016/S0927-0248(00)00295-6

[8] E. R. Shaaban, M. S. Abd El-Sadek, M. El-Hagary, I. S. Yahia, Physica Scripta 86 (1), 015702, (2012); https://doi.org/10.1088/0031-8949/86/01/015702

[9] Chu, L., Chu Shirley, A.: Solid State Electron, 38(1), 533 (1995);

https://doi.org/10.1016/0038-1101(94)00203-R
[10] Chari F. T. and Fadavieslam M. R., Optical and Quantum Electronics, 51(377), 1-16(2019).
[11] Buckingham M. A., Catherall A. L., Hill M. S., Johnson A. L., and Parish J. D., Crystal Growth & Design, 17(2), 907-912(2017); https://doi.org/10.1021/acs.cgd.6b01795
[12] Rodríguez-Mas F., Ferrer J. C., Alonso J. L. and Fernández de Ávila S., Nanomaterials, 9(1212), 1-19 (2019); https://doi.org/10.3390/nano9091212
[13] K. Senthil, D. Mangalraj, S. K. Narayandass, Appl. Surf. Sci.169, 476 (2001); https://doi.org/10.1016/S0169-4332(00)00732-7
[14] P. Taneja, P. Vasa, P. Ayyub, Mater. Lett. 54, 343 (2002); https://doi.org/10.1016/S0167-577X(01)00590-0
[15] ElS Yousef, A. El-Adawy, N. El Koshkhany, E. R.Shaaban, Journal of Physics and Chemistry of Solids., 67(2006)1649-1655; https://doi.org/10.1016/j.jpcs.2006.02.014
[16] M.C. Baykul, A. Balcioglu, Microelectron. Eng. 51, 703 (2000); https://doi.org/10.1016/S0167-9317(99)00534-1
[17] M. Tsuji, T. Aramoto, H. Ohyama, T. Hibino, K. Omura, J. Cryst. Growth 214, 1142 (2000); https://doi.org/10.1016/S0022-0248(00)00291-8
[18] ER Shaaban, YAM Ismail, HS Hassan,Journal of non-crystalline solids 376, 61 (2013); https://doi.org/10.1016/j.jnoncrysol.2013.05.024
[19] R.Padmavathy, N.P. Rajesh, A. Arulchakkaravarthi, R. Gopalakrishnan, P. Santhanaraghavan, P. Ramasamy, Mater. Lett. 53, 321 (2002); https://doi.org/10.1016/S0167-577X(01)00500-6
[20] HH Somaily, Kh S Shaaban, Sayed A Makhlouf, H Algarni, HH Hegazy, EA Wahab, E. R. Shaaban, Journal of Inorganic and Organometallic Polymers and Materials **31**, 138 (2021); https://doi.org/10.1007/s10904-020-01650-2
[21] He, S., Lu, H., Li, B., Zhang, J., Zeng, G., Wu, L., Feng, L., Materials Science in Semiconductor Processing 67 (2017): 41-45; https://doi.org/10.1016/j.mssp.2017.05.009
[22] Qasem, A., Alrafai, H. A., Alshahrani, B., Said, N. M., Hassan, A. A., Yakout, H. A., & Shaaban, E. R., Journal of Alloys and Compounds (2021): 163374; https://doi.org/10.1016/j.jallcom.2021.163374
[23] H. M Rietveld, J. Appl. Crystallogr. 2 (1969) 65-71; https://doi.org/10.1107/S0021889869006558
[24] R. Devi, P. K. Kalita, P. Purakayastha, and B. K. Sarma,. J. Optoelectron. Adv. M., 10(11) (2008) 3077
[25] F. Chen, W. Jie, and X. Cai,. Thin Solid Films 516 (2008) 2823; https://doi.org/10.1016/j.tsf.2007.04.167
[26] J. N. Ximello-Quiebras, G. Contreras-Puente, J. Aguilar-Hernandez, G. Santana-Rodriguez,. and A. Arias-Carbajal Readigos. Sol. Energy Mater. Sol. Cells, 82 (2004) 263; https://doi.org/10.1016/j.solmat.2004.01.023
[27] B. R. Sankapal, R. S. Mane, C. D. Lokhande, Mater. Res. Bull., 35 (2000)177; https://doi.org/10.1016/S0025-5408(00)00210-5
[28] A. L Patterson, Phys. Rev., 56 (1939) 978; https://doi.org/10.1103/PhysRev.56.978
[29] Fouad, O. A., Makhlouf, S. A., Ali, G. A. M., El-Sayed, A. Y.: Mater. Chem. Phys., 128 (2011) 70; https://doi.org/10.1016/j.matchemphys.2011.02.072
[30] K. Senthil, D. Mangalaraj, K. Narayandass, Appl. Surf. Sci., 169-170 (2001) 476; https://doi.org/10.1016/S0169-4332(00)00732-7
'[31] K. Trilok. L.P. Pathak, H.C. Vinod Kumar, Purohit, Swart, R.E. Kroon, Physica E: Low-dimensional Systems and Nanostructures, 84, (2016) 530-536; https://doi.org/10.1016/j.physe.2016.06.020
[32] H. Fujiwara, Spectroscopic Ellipsometry Principles and Applications, John Wiley &Sons Ltd, West Sussex, England, 2007.
[33] M. Emam-Ismail, M. El-Hagary, H. M. El-Sherif, A. M. El-Nagga, M. M. El-Nahass, Opt. Mater. 112 (2021) 110763; https://doi.org/10.1016/j.optmat.2020.110763

[34] M. Emam-Ismail, M. El-Hagary, E. R. Shaaban, S. H. Moustafa, G. M. A. Gad, Ceram. Int. 45 (2019) 8380-8387; https://doi.org/10.1016/j.ceramint.2019.01.146

[35] E. R. Shaaban, M. El-Hagary, M. Emam-Ismail, A. Matar, I. S. Yehia, Mat. Sci. Eng. B 178 (3) (2013) 183-189; https://doi.org/10.1016/j.mseb.2012.11.005

[36] G. E. Jellison, Thin Solid Films. 313-314 (1998) 33-39; https://doi.org/10.1016/S0040-6090(97)00765-7

[37] M. Zhao, R. Tong, X. Chen, T. Ma, J. Dai, J. Lian, J. Ye, Opt. Mater.102 (2020) 109807-109814; https://doi.org/10.1016/j.optmat.2020.109807

[38] Guide to use Complete Ease software manual version (6.51): Data acquisition and analysis software for J.A.Woollam spectroscopic ellipsometers, 2017.

[39] G. A. Niklasson, C. G. Granqvist, O. Hunderi, Appl. Opt.20 (1981)26-30; https://doi.org/10.1364/AO.20.000026

[40] M. Alzaid, W. S. Mohamed, M. El-Hagary, E. R. Shaaban, N. M. A. Hadia, Optical Materials 118 (2021) 111228; https://doi.org/10.1016/j.optmat.2021.111228

[41] J. W. Weber, T. A. R. Hansen, M. C. M. van de Sanden, and R. Engeln, J. Appl. Phys 106, 123503 (2009); https://doi.org/10.1063/1.3257237

[42] S. Tolansky, Multiple-Beam Interference Microscopy of Metals, vol. 55, Academic Press, London, 1970.

[43] T. Bellunato, M. Calvi, C. Matteuzzi, M. Musy, D. L. Perego, B. Storaci, Europ. Phys. J. 52 (2007) 759; https://doi.org/10.1140/epjc/s10052-007-0431-3

[44] K. Senthil, D. Mangalaraj, S.K. Narayandass, and S. Adachi, Mat. Sci. Eng. B, Vol. 78, pp. 53-58, 2000; https://doi.org/10.1016/S0921-5107(00)00510-9

[45] Xiaochun Wu, Fachun Lai, Limei Lin, Jing Lv, Binping Zhuang, Qu Yan, Zhigao Huang, Appl. Surf. Sci. 254 (2008) 6455; https://doi.org/10.1016/j.apsusc.2008.04.023

[46] E. R.Shaaban, M El-Hagary, M Emam-Ismail, MB El-Den, Philosophical Magazine 91 (12) (2011)1679-1692; https://doi.org/10.1080/14786435.2010.544683

[47] Qasem, A., Mostafa, M. S., Yakout, H. A., Mahmoud, M., & Shaaban, E. R., Optics & Laser Technology 148 (2022): 107770; https://doi.org/10.1016/j.optlastec.2021.107770

[48] Qasem, A., Said, N. M., Hassan, A. A., Yakout, H. A., & Shaaban, E. R., Physica B: Condensed Matter (2021): 413600; https://doi.org/10.1016/j.physb.2021.413600

[49] Qasem, A., Hassan, A. A., Rajhi, F. Y., Abbas, H. A. S., & Shaaban, E. R., Journal of Materials Science: Materials in Electronics (2021): 1-13.

[50] J. Tauc, Amorphous and Liquid Semiconductor, New York Plenum, 1974; https://doi.org/10.1007/978-1-4615-8705-7

[51] Qasem, A., Mahmoud, M., Said, N. M., & Rajhi, F. Y., Journal of Inorganic and Organometallic Polymers and Materials (2021): 1-12.

[52] M. S. Bashar, Rummana Matin, Munira Sultana, Ayesha Siddika1, M. Rahaman, M. A. Gafur, F. Ahmed, Journal of Theoretical and Applied Physics 14 (2020)53-63; https://doi.org/10.1007/s40094-019-00361-5

[53] Elsaeedy, H. I., Qasem, A., Mahmoud, M., Yakout, H. A., & Abdelaal, S. A., Optical Materials 115 (2021): 111053; https://doi.org/10.1016/j.optmat.2021.111053

[54] N. El-Kabnay, E. R. Shaaban, N. Afify, A. M. Abou-Sehly, Physica B: Condensed Matter 403 (1) (2008) 31-36; https://doi.org/10.1016/j.physb.2007.08.016

[55] Arenas OL, Nair MTS, Nair PK. Semicond Sci Technol 12 (1997) 1323; https://doi.org/10.1088/0268-1242/12/10/022

[56] Lee J, Lee S, Cho S, Kim S. Mater Chem Phys 77 (2002) 254; https://doi.org/10.1016/S0254-0584(01)00563-6

[57] A. E. Rakhshani and A. S. Al-Azab, J. Phys. Condens. Mater. 12 (2000) 8745; https://doi.org/10.1088/0953-8984/12/40/316

[58] S. A. Al-Kuhaimi, Vacuum, 51 (1998) 349; https://doi.org/10.1016/S0042-207X(98)00112-2

[59] O. Zelaya-Angle, J. J. Alvarado-Gil, R. Lozada-Morales, H. Vargas, A. F. da-Silva, Appl.

Phys. Lett. 64 (1994) 291; https://doi.org/10.1063/1.111184
[60] K. L. Chopra, Thin Film Phenomena, McGraw-Hill, New York, 1969.
[61] H. Oumous and H. Hadiri, Thin Solid Films 386 (2001) 87; https://doi.org/10.1016/S0040-6090(00)01767-3
[62] O.S. Heavens, Optical Properties of Thin Films, Dover, New York, 1965.
[63] M. El-Hagary, E. R. Shaaban, M. Emam-Ismail, S. Althoyaib, J. Alloys compd. 520 (2012) 140-145; https://doi.org/10.1016/j.jallcom.2011.12.160
[64] A. Segura, J. P.Guesdon, J. M. Besson, & A. Chevy, Journal of applied physics 54.2 (1983): 876-888; https://doi.org/10.1063/1.332050
[65] Askari, M., Soltani, N., Saion, E., Yunus, W. M. M., Erfani, H. M., & Dorostkar, M, Superlattices Microstruct. 81 (2015) 193-201; https://doi.org/10.1016/j.spmi.2015.01.011
[66] Xie, R., Su, J., Liu, Y., & Guo, L, Int. J. Hydrog. Energy 39 (7) (2014) 3517-3527; https://doi.org/10.1016/j.ijhydene.2013.12.088
[67] Haeffler, G., Klinkmüller, A. E., Rangell, J., Berzinsh, U., & Hanstorp, D. Molecules and Clusters 38.3 (1996): 211-214; https://doi.org/10.1007/s004600050085
[68] Ferro, R., and J. A. Rodrıguez. Solar energy materials and solar cells 64.4 (2000): 363-370; https://doi.org/10.1016/S0927-0248(00)00228-2
[69] Pawlowski, Lech. The science and engineering of thermal spray coatings. John Wiley & Sons, 2008; https://doi.org/10.1002/9780470754085
[70] Chaibi, W., Peláez, R. J., Blondel, C., Drag, C., & Delsart, C. The European Physical Journal D 58.1 (2010): 29-37; https://doi.org/10.1140/epjd/e2010-00086-7
[71] Lang, Peter F., and Barry C. Smith. Journal of chemical education 80.8 (2003): 938; https://doi.org/10.1021/ed080p938
[72] Bilodeau, René C., Michael Scheer, and Harold K. Haugen. Journal of Physics B: Atomic, Molecular and Optical Physics 31.17 (1998): 3885; https://doi.org/10.1088/0953-4075/31/17/013
[73] Maurya, Ram Charitra. "Appendix I. Inorganic Chemistry. De Gruyter, 2021. 563-576.
[74] Vandevraye, Mickaël, Cyril Drag, and Christophe Blondel. Physical Review A 85.1 (2012): 015401; https://doi.org/10.1103/PhysRevA.85.015401
[75] Bratsch, Steven G., and J. J. Lagowski, Polyhedron 5 (11) (1986) 1763-1770; https://doi.org/10.1016/S0277-5387(00)84854-8
[76] Alshahrani, B., Nabil, S., Elsaeedy, H. I., Yakout, H. A., & Qasem, A., Journal of Electronic Materials (2021): 1-13.
[77] Qasem, A., Mahmoud, M., Elsaeedy, H. I., Mostafa, M. S., & Shaaban, E. R., Optical Materials (2021): 111746; https://doi.org/10.1016/j.optmat.2021.111746
[78] Elsaeedy, H. I., Hassan, A. A., Yakout, H. A., & Qasem, A., Optics & Laser Technology 141 (2021): 107139; https://doi.org/10.1016/j.optlastec.2021.107139
[79] Elsaeedy, H. I., Qasem, A., Yakout, H. A., & Mahmoud, M., Journal of Alloys and Compounds 867 (2021): 159150; https://doi.org/10.1016/j.jallcom.2021.159150